Topologically enabled giant angle-insensitive Goos-Hänchen shift by tunable merging bound states in the continuum of a quasiflat band

Xin Qi,[1] Jiaju Wu,[1] Feng Wu,[2] Mina Ren,[1] Qian Wei,[1] Zhiwei Guo,[1] Haitao Jiang,[1] Yuguang Chen,[1,*] Ya-Ping Yang,[1] Hong Chen,[1] and Yong Sun[1,†]

[1]*MOE Key Laboratory of Advanced Micro-structured Materials, School of Physics Sciences and Engineering, Tongji University, Shanghai 200092, China*

[2]*School of Optoelectronic Engineering, Guangdong Polytechnic Normal University, Guangzhou 510665, China*

(Received 25 January 2024; revised 6 June 2024; accepted 8 July 2024; published 16 July 2024)

Optical bound states in the continuum (BICs) exist commonly in periodic structures with strong local resonances. Merging multiple BICs provides an excellent way to further enhance the Q factor of nearby quasi-BICs compared with isolated BICs. Here, we report on the giant and angle-insensitive transmitted optical Goos-Hänchen shift (GHS) through a photonic crystal slab, assisted by the ultrahigh-Q quasi-BICs on a quasiflat band with embedded tunable merging BICs at a nearly arbitrary wave vector in the reciprocal space. Even at large angles of incidence, GHS can also be enhanced to >4 orders of wavelength by the designed tunable off-Γ merging BICs. Empowered by the angle-insensitive ultrahigh-Q resonances, the wide-angle giant GHS within an extremely narrow bandwidth is realized. Furthermore, we propose an ultrasensitive environmental refractive index sensor and a temperature sensor based on the enhanced GHS by merging BICs. Our work reveals the tremendous potential of tunable merging BICs for various applications based on angular selectivity, such as beam steering, directional vector beams, and angle-multiplexed sensors.

DOI: 10.1103/PhysRevB.110.035420

I. INTRODUCTION

When a light beam launches onto an interface between two different media, it may undergo a lateral shift in the incidence plane. This peculiar shift was observed experimentally by Goos and Hänchen [1], the so-called Goos-Hänchen shift (GHS). Artmann [2] utilized the stationary phase method to explain this phenomenon. Since then, due to its profound physical significance, GHS has attracted tremendous attention in various potential applications, such as optical information storage [3], sensors [4,5], optical switches [6,7], and beam splitters [8]. However, without any external resonance enhanced assistance, the GHS is tiny and usually comparable with the wavelength, which is difficult to monitor. Up to now, there are two main physical mechanisms to significantly enhance the GHS. The first is based on the Brewster effect [9–11]. According to the stationary phase method, the GHS is proportional to the partial derivative of the reflection phase to the incident angle [2]. Thus, using the dramatic changes in the reflection phase angular spectrum near the Brewster angle, the GHS can be enlarged to >1 order of the wavelength [11]. Another common mechanism to enhance GHS is using the optical resonance effect [12], which can also lead to dramatic phase change with incident angle near the resonance angle. According to this resonance mechanism, various resonant microstructures have been proposed to achieve giant GHS, including surface plasmon resonators [13], one-dimensional photonic crystals with defects [14], epsilon-near-zero metamaterial slabs [15], and gradient metasurfaces [16].

Recently, a spatially confined resonance with its energy embedded in a continuous spectrum of propagative modes called the bound state in the continuum (BIC) has attracted researchers' great interest [17–19]. Friedrich and Wintgen [20] proposed the concept of BICs in the context of quantum mechanics. As a result of the universal nature of waves, the BICs have been explored in various fields including quantum mechanics [21,22], acoustic waves [23–25], water waves [26], and electromagnetic waves [27–33]. Various optical platforms such as photonic crystals [34–36] and metamaterials [37] have been used to extensively investigate BICs, due to their structural flexibility and size-dependent spectral scalability. The surprise feature of BICs in photonic crystals and metamaterials is their infinite Q factors even located above the light cone, which is generally considered a leaky mode. Generally, BICs can be divided into two categories: symmetry-protected BICs and accidental BICs. The symmetry-protected BICs usually exist at high-symmetry points in the Brillouin zone [38,39], i.e., the Γ point, where the eigenstate is decoupled with continuous spectra due to symmetry mismatch between the incident plane wave and the structure. An accidental BIC is caused by the destructive interference between the radiation channels of the system and usually occurs at an off-Γ point [40–42]. Therefore, an accidental BIC is no longer dependent on structural symmetry like a symmetry-protected BIC but is sensitive to the geometric parameters of the structure. A perfect BIC can be transformed into a quasi-BIC with a finite Q factor and a finite narrow resonance width, which is also known as a supercavity and can be utilized in many

*Contact author: ygchen@tongji.edu.cn
†Contact author: yongsun@tongji.edu.cn

applications, including sensors [43,44], nonlinear optical devices [45–47], absorbers [48,49], and surface-emitting lasers [50–52]. Due to the presence of quasi-BIC with a sharp asymmetric Fano line shape, the reflection phase undergoes a dramatic change around the incident angle of resonance, offering an efficient approach to enhance the GHS [53–59]. Wu *et al.* [54] exploited a compound grating waveguide structure supporting quasi-BICs to realize giant GHS with unity reflectance. Zheng *et al.* [56] realized enhanced GHS assisted by a symmetry-protected BIC. Du *et al.* [57] observed large transmitted optical GHS in photonic crystal slabs. Although giant GHS can be achieved by a quasi-BIC, the incident angle is strongly limited to a small range. When the incident angle slightly increases, the peak value of GHS will sharply decrease, which is determined by the Q factor of the quasi-BIC [39].

It is worth noting that, even though BICs in optical resonators theoretically exhibit the ideal ability to confine light, in practice, the inevitable scattering losses caused by fabrication imperfections will greatly limit their performance. An excellent way to overcome this shortcoming is to utilize the topological configuration of BICs, which controls the radiative loss of all nearby quasi-BICs [60]. Jin *et al.* [60] revealed that resonances with ultrahigh-Q factors can be achieved through merging multiple BICs, which provides an excellent mechanism to enhance the local field. However, most research on merging BIC has been focused on the Γ point [61,62]. This is not suitable for some applications that require a certain angle of incidence, such as the GHS that occurs when the incident angle is oblique. Kang *et al.* [63,64] implemented merging BICs at the off-Γ point by designing a photonic crystal slab (PhCS) supporting different types of BICs. Very recently, Chen *et al.* [65] demonstrated a remarkable enhancement of GHS assisted by an off-Γ merging BIC. Compared with an isolated BIC, the maximum shift has increased by two orders of magnitude.

In this paper, we theoretically realize giant and angle-insensitive GHS based on tunable merging BICs on a quasiflat band of photonic crystal slab. Empowered by an ultrahigh-Q quasi-BIC on a quasiflat band, the wide-angle giant GHS can be realized as >4 orders of wavelength within an extremely narrow bandwidth. We start from a photonic crystal slab supporting a symmetry-protected BIC at the Γ point and several isolated accidental BICs at an off-Γ point. Then we move four accidental BICs toward the center of the Brillouin zone by varying the periodicity until they merge into a single symmetry-protected BIC, which is pinned at the Γ point if the in-plane inverse symmetry is not broken. When BICs merge at the Γ point, the Q values of nearby resonances (quasi-BICs) are orders of magnitude higher than those of an isolated symmetry-protected BIC. Correspondingly, the robustness of the enhanced GHS assisted by quasi-BICs has also been improved.

One can also force two accidental BICs with opposite topological charges to merge at an off-Γ point by suitably varying the periodicity. Similarly, the merging BICs enhance the Q factors for nearby states compared with the original two isolated BICs. The scaling property changes from $Q \propto k^{-2}$ to $Q \propto k^{-4}$. Therefore, the angle-insensitive GHS enhancement effect can be realized even under large-angle incidence. It is worth noting that just by finetuning the geometry of the unit cell that does not destroy the symmetry, the position of the off-Γ merging BIC can be moved arbitrarily in the ΓX direction, which means that the giant and robust GHS can be achieved at any incident angle. More interestingly, different from the previous works, the manipulation of a BIC and the formation of merging BICs occur on a quasiflat band. Owing to the quasiflat dispersion of a quasi-BIC, the enhanced GHS has a relatively stable operating wavelength in a wide incident angle range. Finally, based on off-Γ merging BICs, we propose an ultrasensitive environmental refractive index sensor and a temperature sensor with a maximum sensitivity of 8.67×10^5 μm/RIU and 2.8×10^6 μm/°C, respectively. This paper opens an avenue for the deployment of merging BICs in building high-performance photonic devices, such as nonlinear metadevices, sensors, and lasers.

II. DESIGN AND MECHANISM

To reveal the topological nature of BICs, we design a square lattice consisting of a C_{4v} dielectric cylinder in a periodic array, as shown in Fig. 1(a). The dielectric cylinder has a height of $h = 338$ nm and a radius of $r = 106$ nm with the refractive index of $n = 3.48$ in the spectral region of interest. The PhCS has a lattice constant of $a = 422$ nm. The band structure of this PhCS is calculated based on the finite-element method (see Appendix A). As shown in Fig. 1(b), there are six bands for the TE mode in which the electric field is confined in the x-y plane in our interested wave band. We will focus on three of them (referred to as TE_1: black, TE_2: red, and TE_3: blue). These bands above the light cone (gray dotted line) show where a continuum of radiative modes in the surrounding material exists. In addition, the mode profiles (H_z) at the Γ point for three bands are shown in the insets. The field distribution of the TE_2 mode we mainly focus on is highly localized in the dielectric column, exhibiting out-of-plane magnetic dipole (MD) resonances. The system has C_2^Z rotation symmetry and up-down mirror symmetry, which altogether ensure that the system supports symmetry-protected BICs and accidental BICs. The red circles in Fig. 1(c) indicate that TE_2 has five BICs with infinite Q factors along $Y\Gamma X$ direction, one of which is a symmetry-protected BIC pinned at the Γ point, while the other four are accidental BICs derived from destructive interference. In comparison, there is only one symmetry-protected BIC on the TE_3 band, as shown in the blue circles. It is also observed that the TE_2 band shows a quasiflat dispersion compared with the nearby TE_1 band; resonance-trapped BICs are associated with flat bands on a band diagram because they have been generated from local resonances, which can be excited via different plane waves and are consequently less sensitive to the direction of the light. The symmetry-protected BIC will remain at the Γ point if the system symmetry is not reduced, whereas the accidental BIC, which does not rely on system symmetry, is easily movable in momentum space by altering structural parameters. Thus, merging BICs may be constructed at any wave vector thanks to the simultaneous existence of multiple different types of BICs on an isolated band, like TE_2. The key for obtaining several BICs and an ultrahigh Q on a single line in k space is to look for multiple accidental BICs on an isolated band.

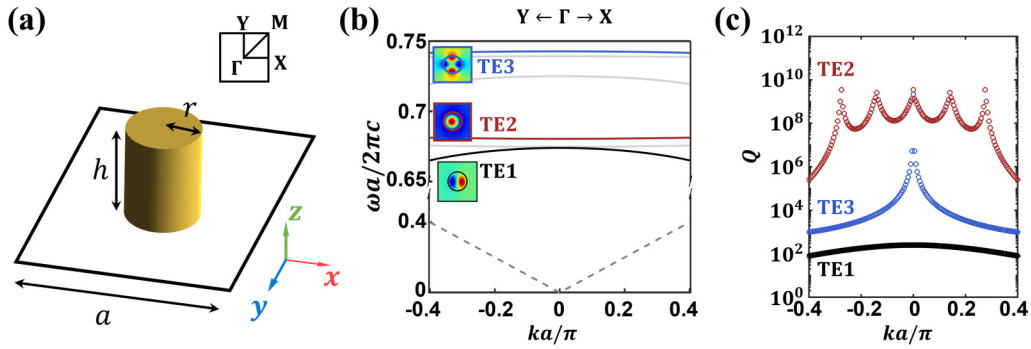

FIG. 1. Band structure and bound state in the continuum (BIC) distribution. (a) Schematic of a unit cell of the proposed photonic crystal slab (PhCS) with the lattice constant $a = 422$ nm. The radius and height of the cylinder are $r = 106$ nm and $h = 338$ nm, respectively. (b) Simulated band structure for TE modes. The TE_1, TE_2, and TE_3 bands are marked in black, red, and blue, respectively. The insets show the mode profiles (H_z) at the Γ point on the $z = 0$ mirror plane. The dashed gray lines represent the light cone. (c) Simulated Q factors of modes for three bands. The Q factors of the TE_2 band show five divergent points along the ΓX direction, which represent one symmetry-protected BIC and four accidental BICs. For band TE_3, there is only one symmetry-protected BIC at the Γ point.

Hu *et al.* [33] proved that an accidental BIC is formed by the interference of the FP and guided modes. The FP modes were previously considered only as background of the spectrum in PhC because of their low-Q factors. There, an accidental BIC is no longer accidental but a common phenomenon associated with the FP mode, providing the possibility to regulate merging BICs.

A. Merging BIC at the Γ point

Figure 2(a) shows the Q factors and polarization vector of far-field radiation on TE_2 in the process of BICs merging at the Γ point. Here, BICs are the bright points in the Q-factor distribution. In addition to the symmetry-protected BIC at the Γ point, several accidental BICs appear surrounding the Γ point at period $a = 422$ nm, as shown in the left panel of Fig. 2(a). The topological charge (q) is defined as the winding number of the polarization vector (C_x, C_y) surrounding a BIC [66], i.e.,

$$q = \frac{1}{2\pi} \oint_C dk \cdot \nabla_k \phi(k). \tag{1}$$

Here, $\phi(k) = \arg[C_x(k) + iC_y(k)]$ is the angle of the polarization, where $C_x(k)$ and $C_y(k)$ denote the electric fields along the x and y directions, respectively, and C is a closed simple path in K space that surrounds the vortex center along the counterclockwise direction. Thus, the vortex or antivortex exhibits a positive or negative topological charge, which is represented by corresponding red or blue solid circles, respectively, as shown in the bottom panels of Fig. 2(a). It can be observed that polarization vortexes emerge around BICs, and the topological charges of the symmetry-protected BIC and accidental BICs are $q = +1$ and ± 1, respectively. It is worth noting that the far-field polarization of a BIC cannot be defined, and there may be calculation errors for the polarization of the ultrahigh-Q states very close to the BIC, as the FEM method does not reach enough convergence (the calculated polarization states for these states around the Γ point in Fig. 2 are inconsistent with C_{4v} symmetry due to the calculation errors). Fortunately, it does not affect the observation of vortex and antivortex phenomena through the polarizations around the BICs. To show the far-field polarization diagrams more clearly, we show the distribution of far-field polarization in an enlarged k space (see Appendix B). The momenta (wave vectors) of topologically protected accidental BICs are tunable under the variation of period a, whereas the symmetry-protected BIC is fixed at the Γ point. As shown in the middle panel of Fig. 2(a), by increasing the period from $a = 422$ to 423.2 nm while maintaining h and r unchanged, four accidental BICs near the Γ point with topological charge $q = -1$ are tuned to merge with the symmetry-protected BIC. The other four BICs, which are far away from the Γ point, move in the opposite direction and deviate from the center of the Brillouin zone. By further increasing period a to 472 nm, the isolated symmetry-protected BIC remains at the Γ point, while these accidental BICs participating in the formation of merging BICs bounce to the ΓM direction, as shown in the right panel of Fig. 2(a). The Q-factor distribution along with the high-symmetry ΓX direction corresponding to different periods a are shown in Fig. 2(b). When the symmetry-protected BIC and accidental BICs coexist at $a = 422$ nm, the Q factor decays roughly as $Q \propto k^{-2}(k^2 - k_{\mathrm{BIC1}}^2)^{-2}(k^2 - k_{\mathrm{BIC2}}^2)^{-2}$ away from the Γ point. Herein, k_{BIC1} and k_{BIC2} are the wave vectors of two accidental BICs with $q = \pm 1$ in the ΓX direction. With the increase of period a, accidental BICs with $q = -1$ gradually approach symmetry-protected BICs and merge at $a = 423.2$ nm. In contrast, a merging BIC has a different scaling rule as $Q \propto k^{-6}(k^2 - k_{\mathrm{BIC}}^2)^{-2}$, which has been significantly enhanced over a broader wave vector range ($|k| < 0.4\pi/a$). When the symmetry-protected BIC is the only preserved BIC near the Γ point, the Q factors decay as $Q \propto k^{-2}$ away from the Γ point. Note that the accidental BICs with $q = +1$ are far from the Γ point, and thus, the contribution of this accidental BICs to Q factors in the area discussed above can be ignored in this case.

B. Robust GHS by Γ-merging BIC

By utilizing a merging BIC on a flat band, robust enhanced GHS can be achieved. At $a = 423.2$ nm, several BICs merge at the Γ point on the TE_2 band, while there is a single symmetry-protected BIC on the TE_3 band [see in Fig. 1(c)].

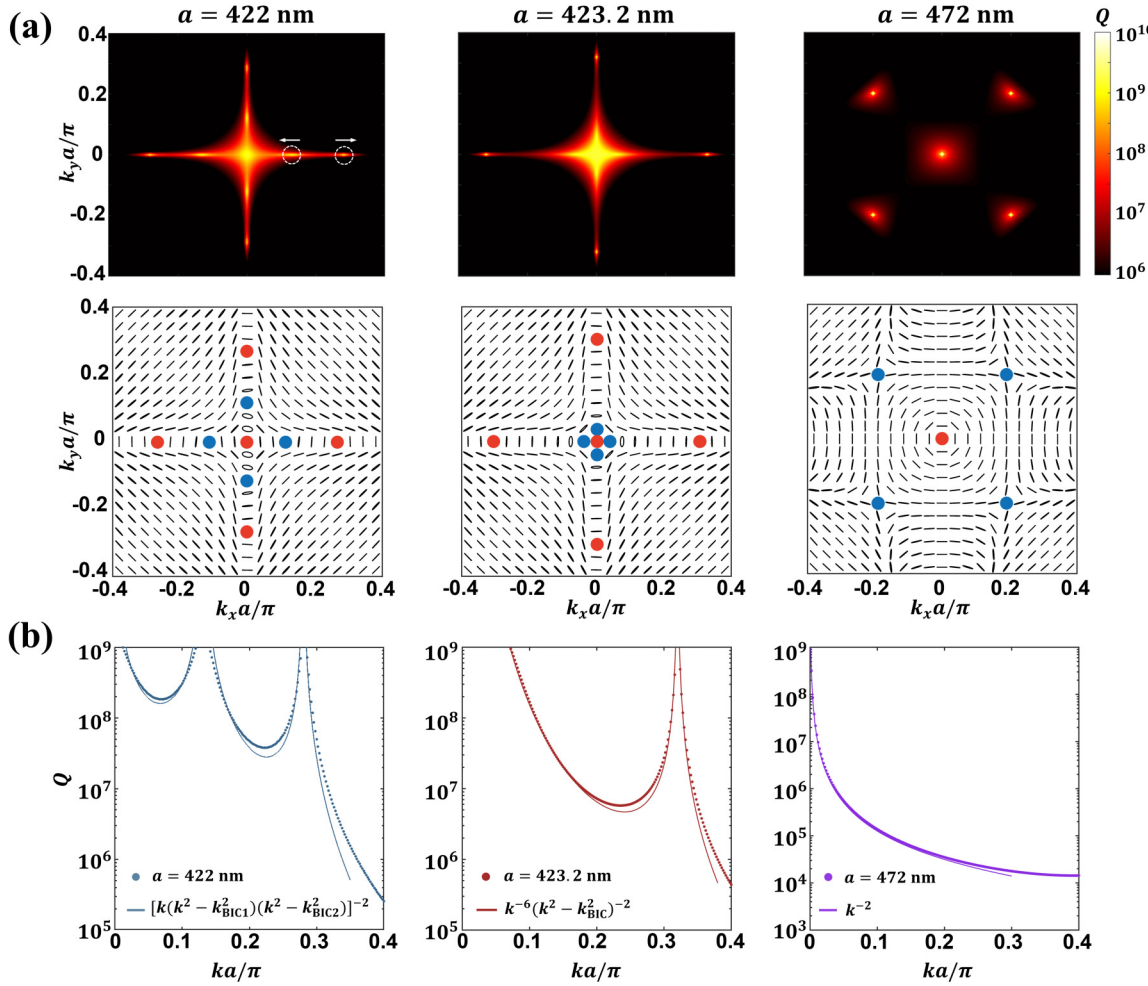

FIG. 2. Merging bound states of the continuum (BICs) at the Γ point. (a) Three panels on top present the simulated Q factors of the TE_2 band for photonic crystal slabs (PhCSs) with different periods a. The white circles and arrows indicate the accidental BICs and their moving direction with increasing a, respectively. Below are the corresponding far-field polarization diagrams. The blue and red dots represent BICs with topological charges of -1 and $+1$, respectively. When a is tuned from 422 to 423.2 nm, four accidental BICs with topological charge -1 merge with a symmetry-protected BIC with charge $+1$. Further increasing a, accidental BICs will deflect in the ΓM direction. (b) Simulated Q factors (dotted lines) and the corresponding fitting curves (solid lines). The Q factors before ($a = 422$ nm) and after ($a = 472$ nm) BICs merge are marked as blue and magenta, respectively. The intermediate transient process ($a = 423.2$ nm) is merging BICs, marked as red. Compared with isolated BICs, the merging BICs significantly enhances the Q factors of the nearby states, which satisfy the rule $Q \propto k^{-6}$ in the vicinity of the Γ point.

The numerically simulated reflectance spectra of a quasi-BIC by sweeping the incident angle θ are given in Figs. 3(a) and 3(b). The incident wave is an oblique incident TE plane wave whose polarization direction is in the y direction. The quasi-BICs evolved from an isolated BIC are almost obscured by the surrounding background when θ reaches 15°, while those evolved from merging BICs maintain an extremely narrow linewidth, which exhibits an excellent ability for wide-angle GHS enhancement. According to the stationary phase method, the lateral GHS for the reflected beam with a sufficiently large beam waist can be determined by [2,54]

$$S_{GH} = -\frac{\lambda_0}{2\pi}\frac{\partial \varphi_r}{\partial \theta}, \tag{2}$$

where φ_r denotes the reflection phase, and the GHS is proportional to the partial derivative of the reflection phase.

For comparison, we first calculate the GHS enhanced by a single BIC on TE_3 with fixing the incident wavelength

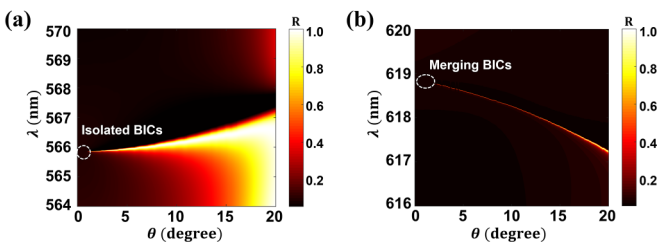

FIG. 3. Angle-insensitive ultrahigh-Q resonance. (a) Simulated reflection spectra of an isolated symmetry-protected bound state in the continuum (BIC) on TE_3 by sweeping incident angle θ from 0° to 20°. (b) Simulated reflection spectra of merging BICs at the Γ point on TE_2 by sweeping θ from 0° to 20°.

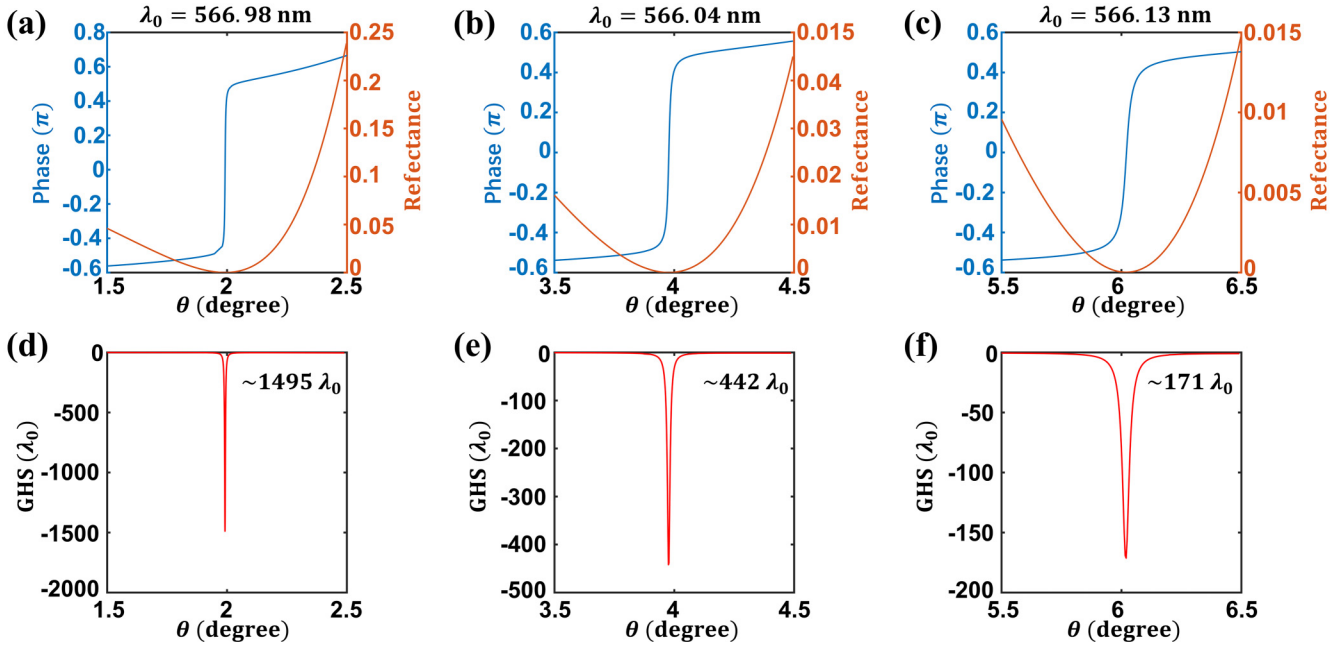

FIG. 4. Enhanced Goos-Hänchen shift (GHS) assisted by an isolated symmetry-protected bound state in the continuum (BIC). The reflectance angular spectra (orange line) and phase angular spectra (blue line) for (a) $\lambda_0 = 566.98$ nm, (b) $\lambda_0 = 566.04$ nm, and (c) $\lambda_0 = 566.13$ nm. The GHS angular spectra around the incident angle (d) $\theta = 2^\circ$ for $\lambda_0 = 566.98$ nm, (e) $\theta = 4^\circ$ for $\lambda_0 = 566.04$ nm, and (f) $\theta = 6^\circ$ for $\lambda_0 = 566.13$ nm.

(denoted by λ_0) near resonance. By sweeping the incident angle, we obtain the reflectance angular spectra (red line) and reflection phase angular spectra (blue line), as shown in Figs. 4(a)–4(c). The reflection phase changes drastically around $\theta = 2^\circ$, 4°, and 6°, respectively, which is located at the minimum of reflectance, indicating a transmitted optical GHS. The corresponding peak value of the GHS caused by acute change of phase is achieved at incident angles $\theta = 2^\circ$, 4°, and 6°, as shown in Figs. 4(d)–4(f), respectively. It is obvious that the peak value (absolute value) of GHS decreases sharply from $\sim 1495\lambda_0$ to $171\lambda_0$ as θ increases from 2° to 6°. The significant weakening of the enhancement effect is due to the rapid decline of the Q factor of a quasi-BIC.

For the case of merging BICs on TE_2 (when $a =$ 423.2 nm), the reflectance angular spectra and phase angular spectra are similarly calculated with different λ_0's, as shown in Figs. 5(a)–5(c). One can see that the reflection phase changes drastically around incident angles $\theta = 5^\circ$, 10°, and 15°, respectively, when $\lambda_0 = 618.6$, 618.3, and 617.8 nm. The position where the phase drops sharply corresponds to the minimum value of reflection, which also means a transmitted optical GHS. Due to multiple BICs merging at the Γ point, the Q factors of quasi-BICs have been greatly improved, enabling sharp reflection resonance to be achieved in a wide range of incident angles. The corresponding GHS angular spectra are subsequently calculated, as shown in Figs. 5(d)–5(f), respectively. Compared with shift enhancement effect assisted by a single BIC [see in Figs. 4(d)–4(f)], giant GHS empowered by merging BICs is no longer sensitive to incident angle. When incident angle θ starts at 5°, the maximum GHS is $\sim 4530\lambda_0$. As θ increases to 10°, the maximum GHS remains at $3355\lambda_0$. Finally, when θ comes to 15°, the maximum GHS reaches as high as $2442\lambda_0$, which can still be enhanced to >3 orders of wavelength.

Insensitivity to the incident angle is not only manifested in the maximum value of GHS but also in the operating wavelength. Since a merging BIC is designed on a flat band, the resonance wavelength has very small dispersion, which makes the incident wavelength of realizing huge GHS basically unchanged at different incident angles. As θ increases from 5° to 20°, the relative shift of quasi-BIC mode $\Delta\lambda/\lambda_1$ is equal to 0.2%, as shown in Fig. 3(b), where $\Delta\lambda$ is the resonance wavelength shift, and λ_1 is the wavelength when $\theta = 5^\circ$. Therefore, enhanced GHS over a wide-angle range is achieved with very little changes in the operating wavelength.

To show the robustness of enhanced GHS clearly, we give the variation of the peak value of the GHS as incident angle θ changes under different BICs in Fig. 6. For a single symmetry-protected BIC, when $\theta = 10^\circ$, the peak value of GHS is just $\sim 6.7 \times 10^1\lambda_0$, as shown by the blue circles in Fig. 6. As θ gradually approaches zero, the peak value of GHS increases greatly. For example, when $\theta = 1^\circ$, the maximum GHS reaches $\sim 3.6 \times 10^3\lambda_0$. It is indicated that the enhancement of the GHS is directly related to the Q factor of the quasi-BIC. Unlike the enhancement effect of a single BIC, the GHS enhanced by a merging BIC does not decrease sharply with increasing incident angle (see the red circles in Fig. 6). The gray area in Fig. 6 represents the range of merging BICs. When the incident angle increases to a certain extent, such as $\theta = 4^\circ$, the merging BICs transform into a quasi-BIC with ultrahigh Q, which results in a giant GHS $\sim 5.2 \times 10^3\lambda_0$. Even if the incident angle θ increases to 20°, the peak value of GHS remains >3 orders of wavelength as $\sim 2 \times 10^3\lambda_0$, which is much higher than the almost vanishing enhancement assisted by a single BIC.

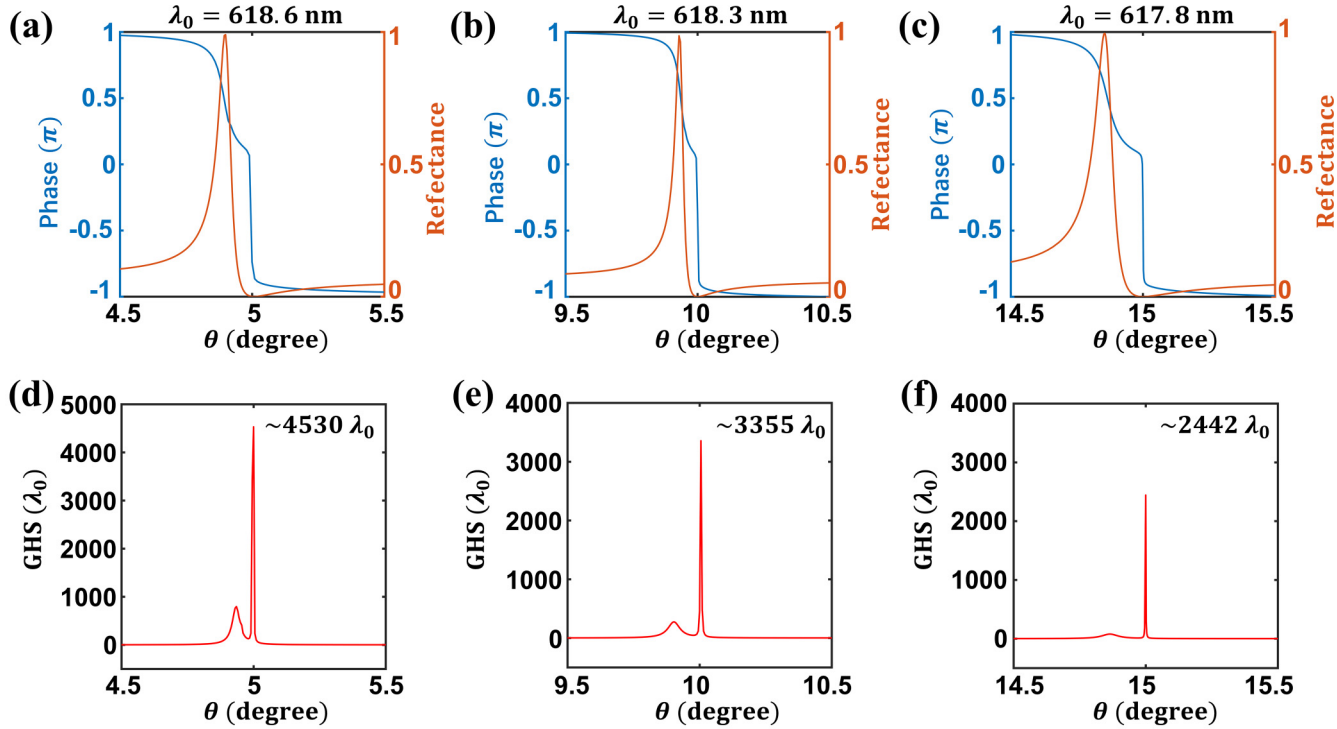

FIG. 5. Enhanced Goos-Hänchen shift (GHS) assisted by merging a bound state in the continuum (BIC) at the Γ point. The reflectance angular spectra (orange line) and phase angular spectra (blue line) for (a) $\lambda_0 = 618.6$ nm, (b) $\lambda_0 = 618.3$ nm, and (c) $\lambda_0 = 617.8$ nm. The GHS angular spectra around the incident angle (d) $\theta = 5^\circ$ for $\lambda_0 = 618.6$ nm, (e) $\theta = 10^\circ$ for $\lambda_0 = 618.3$ nm, and (f) $\theta = 15^\circ$ for $\lambda_0 = 617.8$ nm.

C. Merging BIC at an off-Γ point

Compared with the merging BICs at the Γ point, the merging BICs at an off-Γ point are more meaningful for GHS, which requires oblique incidence. If we decrease period a from 422 nm, two off-Γ accidental BICs located at the TE_2 band [see in Fig. 2(a)] will approach each other along the ΓX (ΓY) direction. When $a = 421.1$ nm, they meet at an off-Γ point, and merging BICs occur, as indicated in the left panel of Fig. 7(a). The white arrows denote the moving direction of accidental BICs. Note that, whether constructing merging BICs at the Γ or an off-Γ point, only changing the period does not break the symmetry of the structure. Two accidental merged BICs have opposite topological charges. The polarization field near the BIC characterizes the positive and negative topological charges [see the bottom panel of Fig. 7(a)]. With further decreasing a to 420.5 nm, these two accidental BICs will undergo annihilation. BICs transform into quasi-BICs, where the Q factors are not infinite but remain large, which can be regarded as a supercavity, as shown by the dash circle area in right panel of Fig. 7(a). We also give the corresponding simulated Q-factor distribution in the ΓX direction, as shown in Fig. 7(b), indicating that the Q factors near merging BICs (left panel) follow the scaling rule as $Q \propto k^{-2}(k^2 - k_{\mathrm{BIC}}^2)^{-4}$, which is significantly enhanced over a broad wave vector compared with either an isolated symmetry-protected BIC or an isolated accidental BIC. To further verify the authenticity of the abovementioned merged BIC, we calculated the reflection angle spectrum to ensure that the two accidental BICs did annihilate each other. The specific results are shown in Appendix C. The Q factors are dominated by the intrinsic loss of materials at merging BICs, and thus, high-refractive-index dielectric material with ultralow intrinsic loss is an appropriate choice to create a high-Q cavity (see Appendix D). We also discuss the impact of perturbations in lattice constant a on the quality factor of the merging quasi-BICs (see Appendix E).

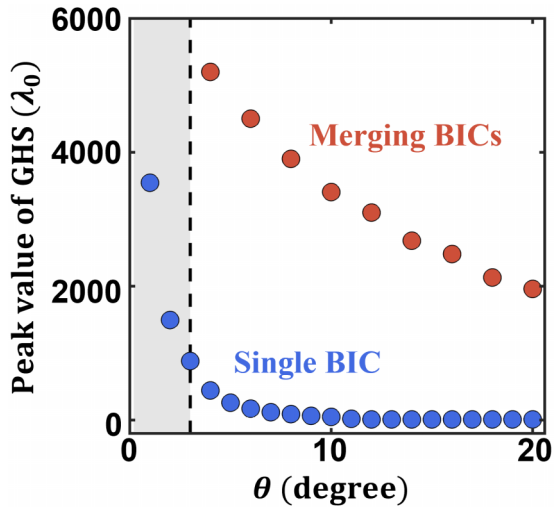

FIG. 6. Dependence of peak value of Goos-Hänchen shift (GHS) enhanced by (a) a single bound state in the continuum (BIC) and (b) merging BICs on incident angle θ.

Next, we show that off-Γ merging BICs can be achieved at an arbitrary point along the ΓX direction in the reciprocal

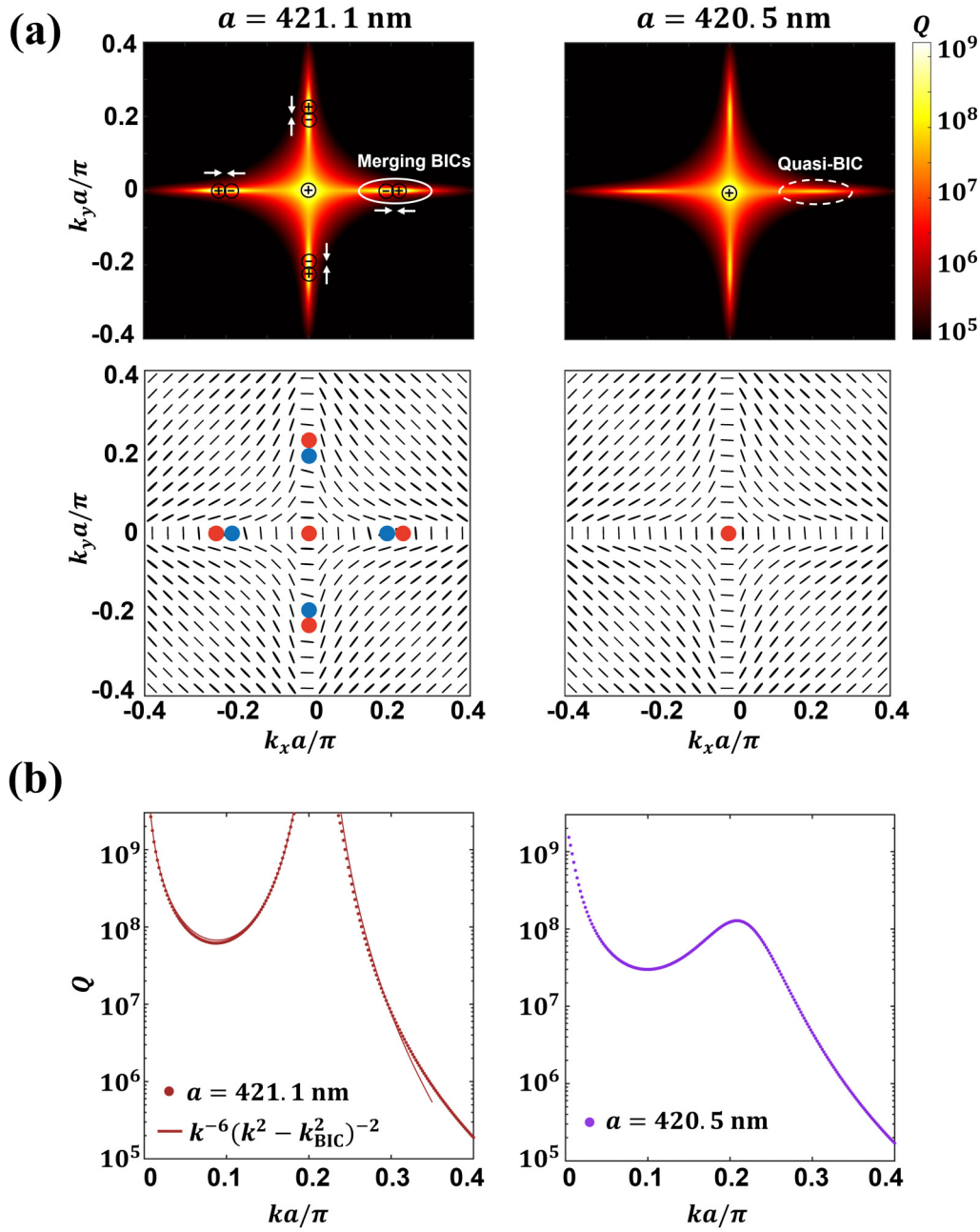

FIG. 7. Merging bound states in the continuum (BICs) at an off-Γ point. (a) Above is the simulated Q factor of the TE_2 band in different periods a. The white arrows indicate the moving direction of accidental BICs. Below is the corresponding far-field polarization diagram. The blue and red dots represent BIC with topological charges of -1 and $+1$, respectively. When a is tuned from 422 to 421.1 nm, the two accidental BICs with opposite topological charges approach to each other and form merging BICs at an off-Γ point. Further decreasing a, the two BICs annihilate and evolve into a quasi-BIC. (b) Simulated Q factors (dotted lines) and fitting curves (solid lines). The Q factors before ($a = 422$ nm) and after ($a = 420.5$ nm) BICs merge are marked as red and magenta, respectively. The merging BICs case has considerably enhanced Q factors for nearby states compared with the isolated BIC case as the dependence of the Q factor on the wave vector near BICs changes from k^{-2} to k^{-4}. Even if the two BICs collide and annihilate with each other, the converted quasi-BIC still maintains a high-Q factor.

space by concurrently modifying the period a and height h while maintaining C_4^z symmetry. The sensitivity of two accidental BICs with opposite topological charges to different parameter tunings is different (see Appendix F). Specifically, the two accidental BICs move in the momentum space at nearly the same speed for changes in period a. However, compared with the accidental BIC with topological charge $+1$, the accidental BIC with topological charge -1 is much more sensitive to the height h, which means that, by varying the height h, different accidental BICs have different moving scales Δk_{BIC}. That could be explained by the fact that, when changing the height of dielectric pillar, the resonance frequency shift of FP modes is different. The frequency shift of the higher-order FP mode is more sensitive to height h, so the asymmetric moving speeds are present in the accidental BICs originating from the coupling of the MD mode and

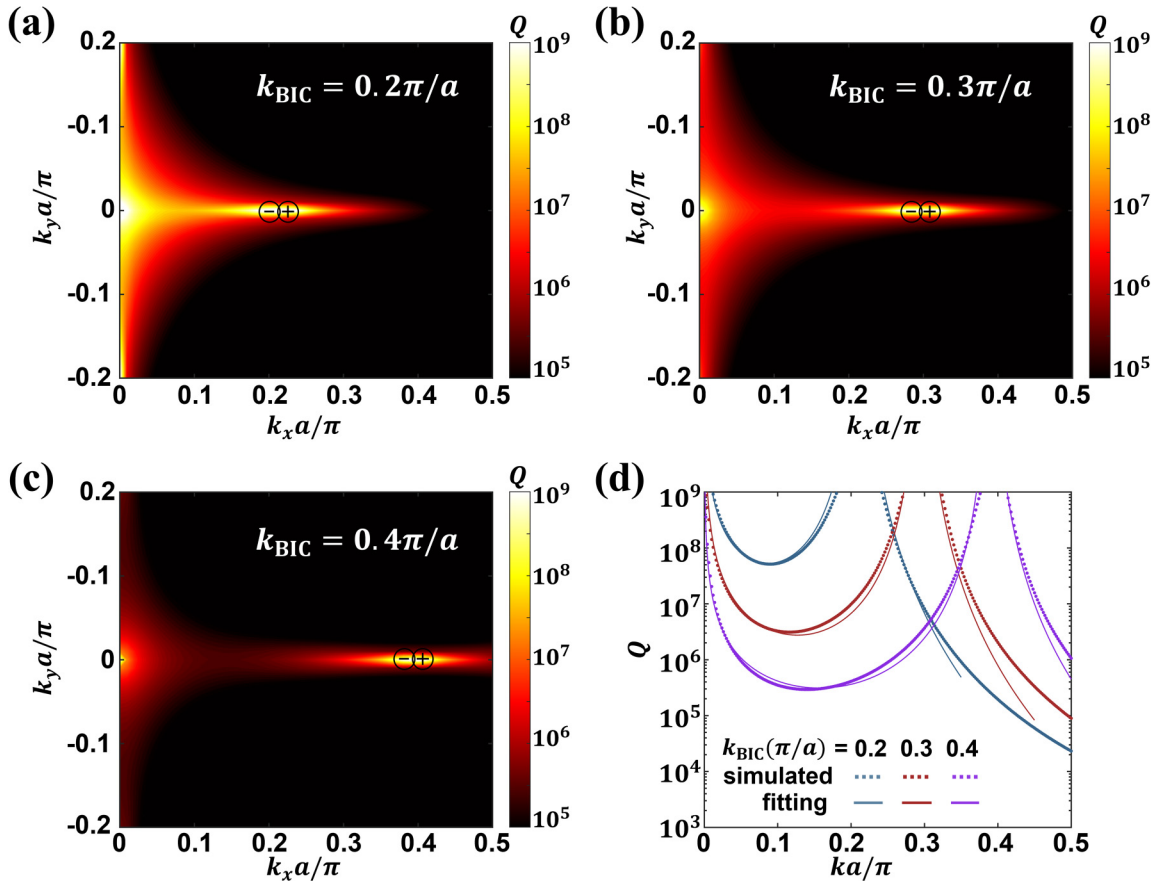

FIG. 8. Tunable merging bound states in the continuum (BICs). Simulated polarization vectors (white arrows) around the accidental BICs at different wave vectors with the Q factors as the background color for the TE_2 band. The wave vector of merging BICs at (a) $0.2\pi/a$, (b) $0.3\pi/a$, and (c) $0.4\pi/a$; corresponding (a, h) parameters are (421.38 nm, 338.4 nm), (432.1 nm, 340 nm), and (445 nm, 342.8 nm), respectively. By properly selecting parameters a and h, merging BICs can be realized at almost any wave vector position. (d) Simulated Q factors (dotted lines) and fitting curves (solid lines) corresponding to merging BICs at different wave vectors. The merging BICs located at arbitrary wave vector follow the scale ruling as $Q \propto k^{-2}(k^2 - k_{BIC}^2)^{-4}$.

different orders of the FP mode [33]. Therefore, the merging BICs can be designed at an arbitrary off-Γ point if the proper period a and height h are chosen. For example, when $(a, t)'$s are equal to (421.38 nm, 338.4 nm), (432.1 nm, 340 nm), and (445 nm, 342.8 nm), merging BICs are tuned to $k_x = 0.2\pi/a$, $0.3\pi/a$, and $0.4\pi/a$, respectively [see in Figs. 8(a)–8(c)]. The Q factors in these three scenarios satisfy the scaling rule $Q \propto k^{-2}(k^2 - k_{BIC}^2)^{-4}$, which proves the existence of a merging BIC, as shown in Fig. 8(d).

D. Robust GHS by off-Γ merging BIC

To demonstrate the enhancement of GHS by an off-Γ merging BIC, we designed merging BICs at 15° with $a =$ 442 nm, $r = 106$ nm, and $h = 342$ nm. Figure 9(a) shows the variation of Q factors with incident angle. The Q factor diverges at 0° and 15°, which is due to the existence of a symmetry-protected BIC and off-Γ merging BICs. From the reflection angular spectrum, it can be clearly observed that the linewidths at two places disappear, as shown in Fig. 9(b). The quasi-BIC near merging BICs has an ultrahigh Q, which makes it possible to realize giant GHS in a larger angle range. At different wavelengths λ_0, we calculated the GHS of the peak at 5°, 10°, 20°, and 25°, as shown in Figs. 9(c) and 9(d), respectively. The reflectance angular spectra and reflection phase angular spectra are also given in Appendix G. The peak values of GHS are all $\sim 3.0 \times 10^3 \lambda_0$, demonstrating great robustness to angles. This is consistent with the characteristic that a merging BIC can enhance the Q factors of nearby quasi-BICs. Moreover, when the resonance peak shifts from 5° to 25°, the relative shift of the resonance wavelength is only 0.26%. Therefore, off-Γ merging BICs can achieve wide angle GHS enhancement at a larger incident angle within an extremely narrow bandwidth.

As mentioned above, off-Γ merging BICs can be designed at an arbitrary wave vector by choosing a suitable period a and height h. This provides an excellent mechanism for realizing enhanced GHS at arbitrary angles. Figure. 10(a)–10(c) show the enhancement of GHS by a merging BIC at 5°, 10°, and 15°, respectively. The corresponding structure parameters (a, h) are (425.78 nm, 339.04 nm), (440.08 nm, 341.12 nm), and (453.25 nm, 343.06 nm), respectively. The radius equals 106 nm and remains unchanged. Regardless of the angle at which the merging BICs are designed, the peak value of GHS remains $>3.0 \times 10^3 \lambda_0$ within a range of 10° near the merging BICs. It is worth mentioning that there is a

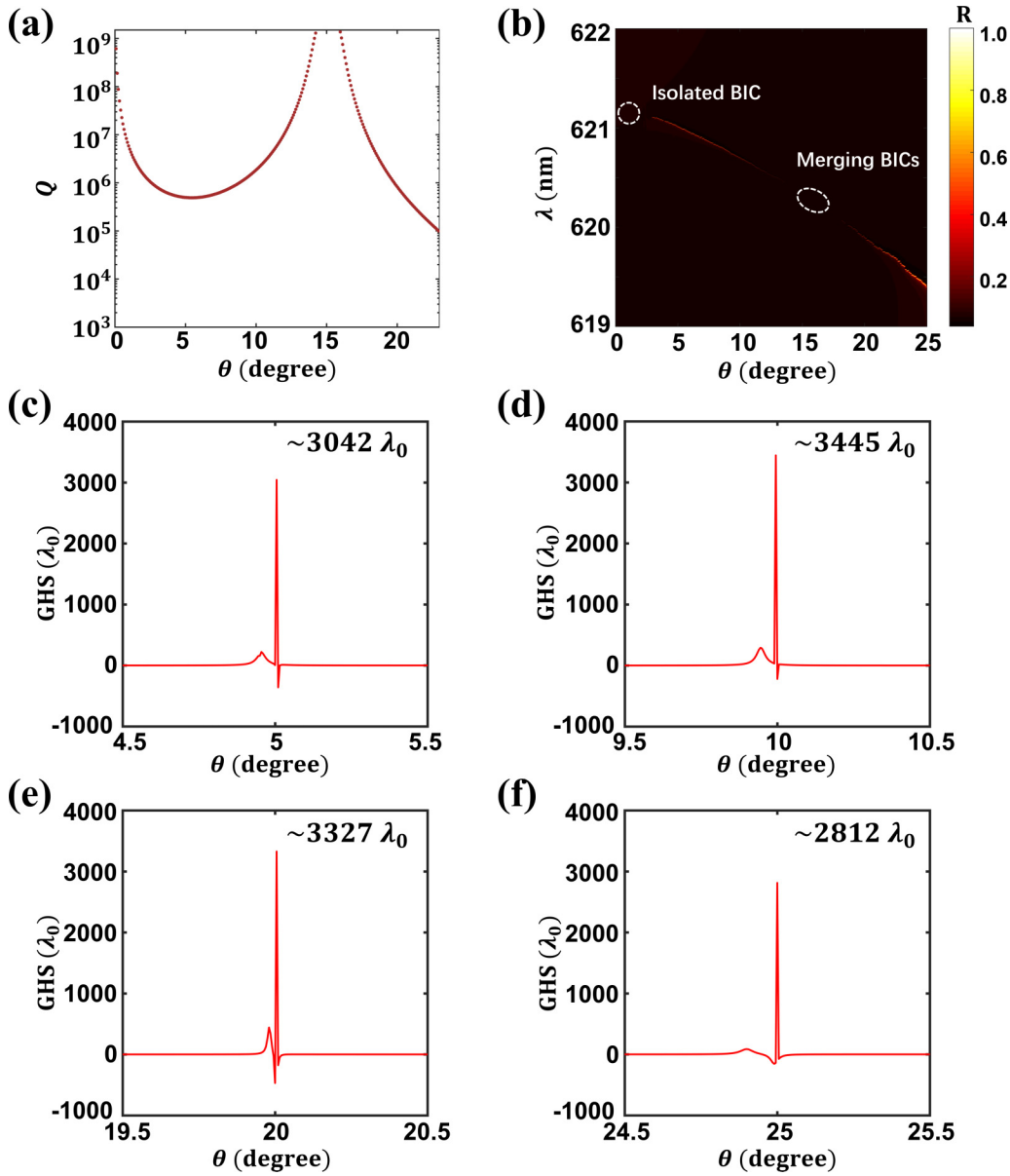

FIG. 9. Angle-insensitive Goos-Hänchen shift (GHS) enhanced by off-Γ merging bound states in the continuum (BICs). (a) Dependence of the peak value of GHS on the incident angle. (b) Reflection spectra of merging BICs at an off-Γ point by sweeping θ from 0° to 25°. The GHS angular spectra around the incident angle (c) $\theta = 5°$ for $\lambda_0 = 621.05$ nm, (d) $\theta = 10°$ for $\lambda_0 = 620.71$ nm, (e) $\theta = 20°$ for $\lambda_0 = 619.82$ nm, and (f) $\theta = 25°$ for $\lambda_0 = 619.38$ nm.

symmetry-protected BIC at the Γ point, which can improve the Q factors of quasi-BICs near Γ. Therefore, the smaller the angle of off-Γ merging BICs (closer to the Γ point), the greater the influence of a symmetry-protected BIC on the GHS enhancement near it. Specifically, the peak value of GHS near the merging BICs at 10° in Fig. 10(a) is slightly higher than that at 15° and 20°, as shown in Figs. 10(b) and 10(c), respectively.

E. Refractive index sensor based on giant GHS

Utilizing the exceptional sensitivity of GHS, an ultrasensitive refractive index sensor was designed based on ultrahigh-Q quasi-BICs near off-Γ BICs. Here, we consider the PhCS with off-Γ merging BICs at 10°, as above [see in Fig. 10(a)].

The structural parameters are $a = 425.78$ nm, $r = 106$ nm, and $h = 339.04$ nm. We investigate the influence of a slight change of the refractive index n around PhCS on its reflectivity under the oblique incidence of a TE-polarization wave, as shown in Fig. 11(a). The calculated reflection angular spectra at a fixed wavelength $\lambda_0 = 619.17$ nm demonstrate that a tiny change of the surrounding refractive index leads to an offset of the reflectance peak in angular spectra. Moreover, the peak value of GHS also deviates around the incident angle of resonance. Figure 11(b) shows the dependence of the peak value of GHS on the environmental refractive index n. As n varies from 1 to 1.001, the peak value of GHS reduces from $3571\lambda_0$ to $2138\lambda_0$, which can serve as a basis for designing sensors. The maximum GHS with the variation of refractive index is visually depicted in Fig. 11(c). The sensitivity of the proposed

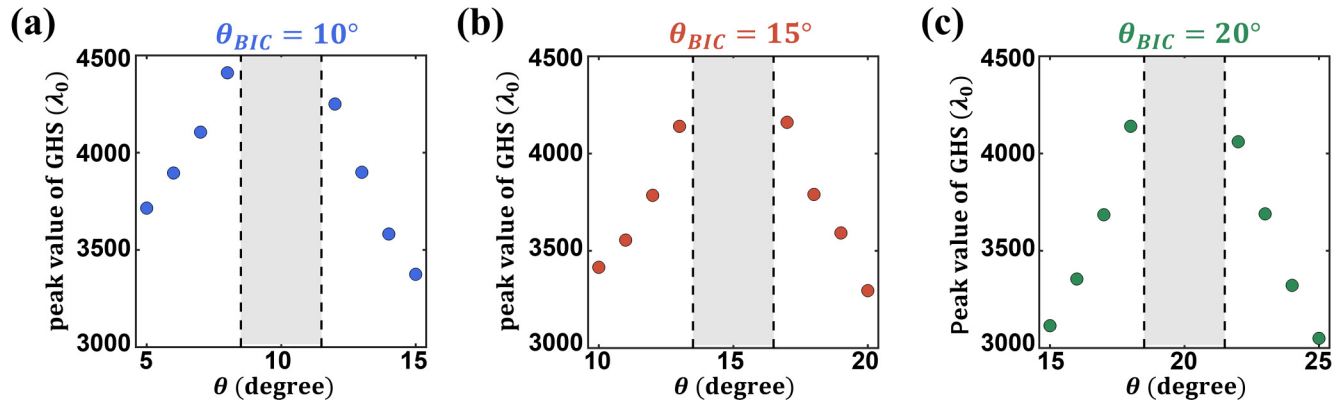

FIG. 10. Design giant Goos-Hänchen shift (GHS) at an arbitrary angle. Dependence of the peak value of GHS enhanced by off-Γ merging bound states in the continuum (BICs) at (a) $\theta_{\mathrm{BIC}} = 10°$, (b) $\theta_{\mathrm{BIC}} = 15°$, and (c) $\theta_{\mathrm{BIC}} = 20°$. The corresponding structure parameters (a, h) are (425.78 nm, 339.04 nm), (440.08 nm, 341.12 nm), and (453.25 nm, 343.06 nm), respectively.

sensor can be defined as the derivative (absolute value) of the maximum GHS concerning the refractive index, that is,

$$S = \left| \frac{dS_{\mathrm{GH}}}{dn} \right|. \tag{3}$$

We can perform a linear fit of the dependence of the maximum GHS on refractive index n, as denoted by the red dashed line in Fig. 11(c). The proposed sensor has a maximum sensitivity of 8.67×10^5 μm/RIU, indicating that it can be used to detect extremely tiny variation of environmental refractive index, such as climate monitoring [67], biochemical detection [68], and foreign object detection [69].

F. Ultrasensitive temperature sensor based on giant GHS

Similarly, an ultrasensitive temperature sensor can also be designed based on the above off-Γ merging BIC-assisted giant GHS. As an alternative temperature-sensitive dielectric

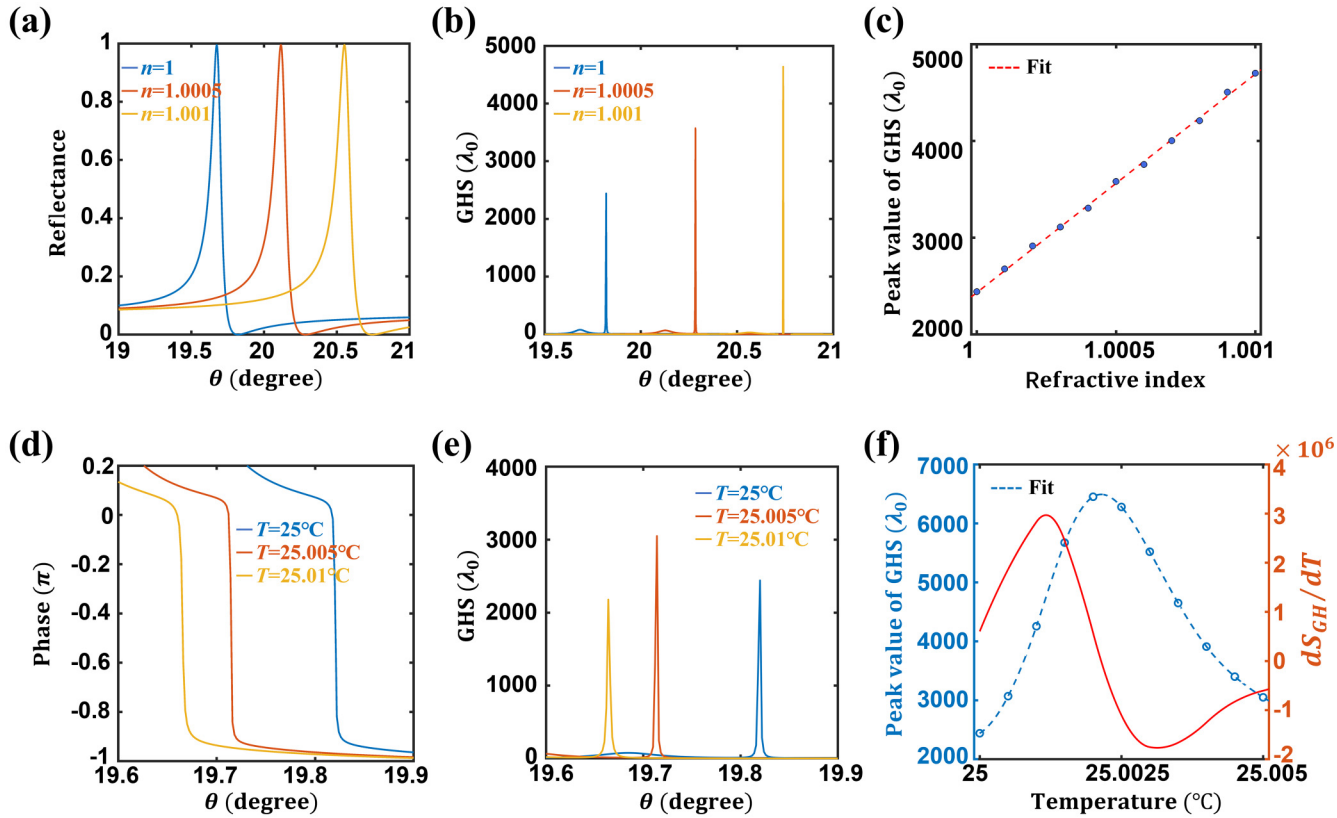

FIG. 11. Design sensors with merging bound states in the continuum (BICs). (a) The reflectance angular spectra and (b) Goos-Hänchen shift (GHS) at different environmental refractive index n. (c) The GHS of the proposed sensor as a function of the environmental refractive index n. The red dashed line represents a linear fit. (d) The reflection phase and (e) GHS at different temperatures. (f) Temperature-dependent sensitivity of the proposed sensor.

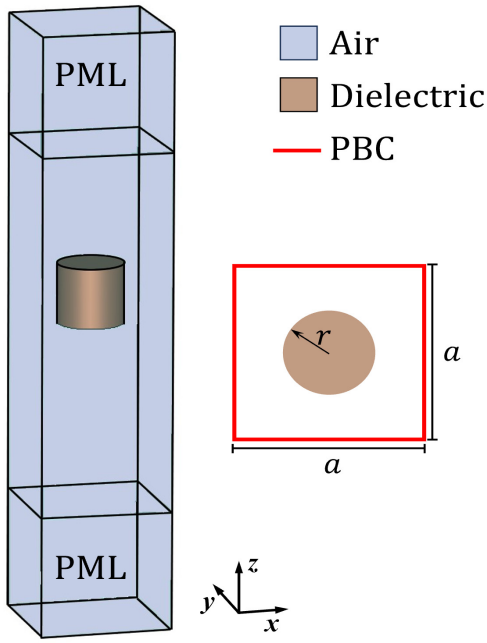

FIG. 12. Computational domain of the proposed structure with $r = 106$ nm and $h = 338$ nm, lattice constant $a = 422$ nm, and corresponding boundary conditions used. The color scheme represents the material choice, air, and dielectric material, simulated with their respective refractive index.

material, GaAs has relatively high index [70] and thermo-optical coefficient [71]. Here, we choose it as the high-index medium for a cylinder and still choose the PhCS with off-Γ merging BICs at 10°, as above [see in Fig. 10(a)]. The temperature-dependent refractive indices of GaAs can be expressed in $n(T) = n(T_0) + \alpha(T - T_0)$, where $T_0 = 25°\text{C}$ is the room temperature, $n(T_0) = 3.48$ [70], and $\alpha = 2.3 \times 10^{-4}/°\text{C}$ is the thermo-optical coefficient. The geometric parameters at room temperature are designed to be $r(T_0) = 106$ nm and $h(T_0) = 339.04$ nm. Considering the thermal expansion effect, the temperature-dependent geometric parameters can be given by $r(T) = [1 + \beta(T - T_0)]r(T_0)$ and $h(T) = [1 + \beta(T - T_0)]h(T_0)$, where $\beta = 7 \times 10^{-6}/°\text{C}$ [68]. We investigate the influence of a slight change of the

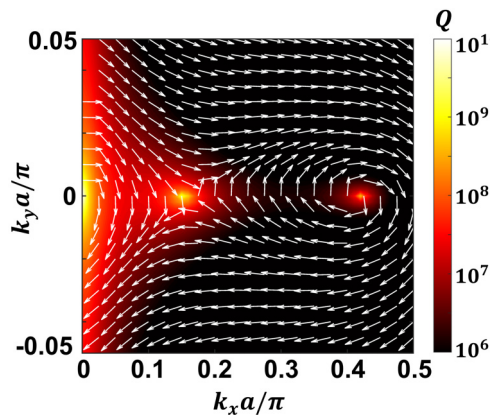

FIG. 13. The far-field polarization plotted along the long axis of the ellipse polarization in an enlarged k space.

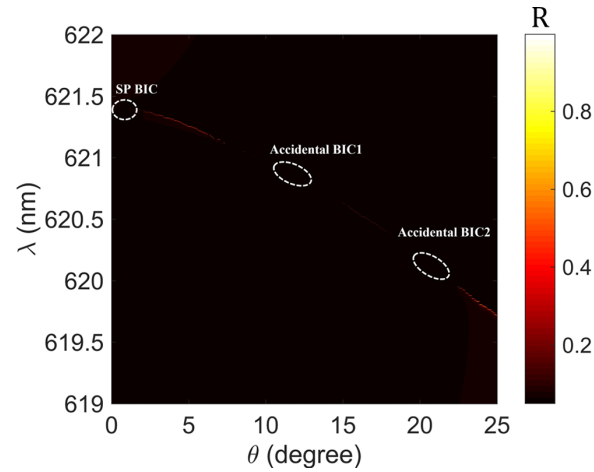

FIG. 14. Reflection angle spectra before merge by sweeping incident angle θ from 0° to 25°.

temperature T on the reflection phase under the oblique incidence of a TE-polarization wave, as shown in Fig. 11(d). The calculated reflection phases at a fixed wavelength $\lambda_0 = 619.17$ nm indicate that the position where the phase sharply drops shifts in the angular spectrum with slight increase of temperature. Figure 11(e) shows the dependence of the peak value of GHS on the temperature. As n varies from 25 to 25.01°C, the peak value of GHS will change nonlinearly, which can serve as a basis for designing sensors.

The sensitivity of a temperature sensor can be defined as the derivative (absolute value) of the maximum GHS concerning the temperature, that is, $|dS_{\text{GH}}/dT|$. The maximum GHS with the variation of temperature and the sensitivity of the proposed sensor are visually depicted in Fig. 11(f). The proposed ultrasensitive temperature sensor has a maximum sensitivity of 2.8×10^6 μm/°C, which means that it can be used to monitor very small temperature changes.

III. CONCLUSIONS

In summary, we proposed a feasible mechanism to construct merging BICs at almost arbitrary points in momentum space on a quasiflat band. Compared with an isolated symmetry-protected BIC, the GHS assisted by merging BICs at the Γ point can be further greatly enhanced in a wide range of incident angles. Moreover, because the movement of BICs and the formation of merging BICs occur on a quasiflat band, the tiny dispersion makes the operating frequency of enhanced GHS also insensitive to the incident angle. Therefore, the wide-angle giant GHS in extremely narrow bandwidth is realized. We have also implemented this robust and giant GHS by constructing tunable off-Γ merging BICs, which allows the GHS enhancement to occur at larger oblique incident angles. Finally, based on the giant GHS assisted by merging BICs, an environmental refractive index sensor and a temperature sensor are proposed with a maximum sensitivity of 8.67×10^5 μm/RIU and 2.8×10^6 μm/°C, respectively. This paper has opened a path for the application of merging BICs in the construction of high-performance photonic devices such as nonlinear metadevices, sensors, and lasers.

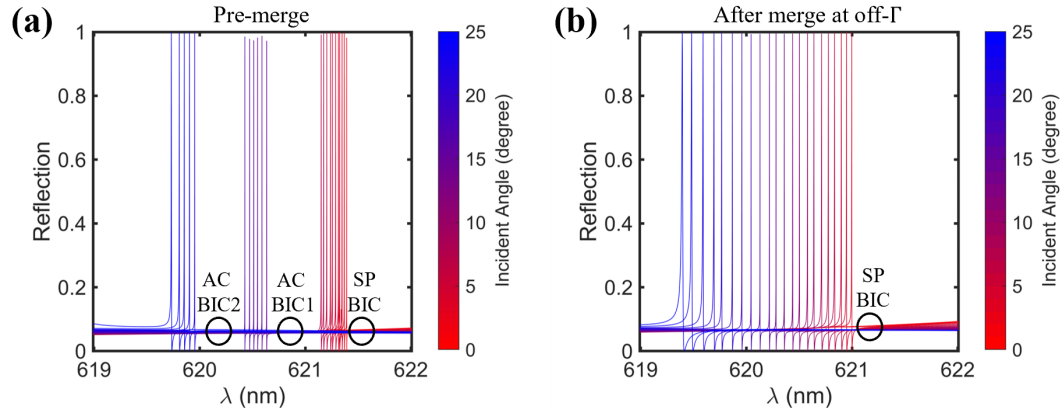

FIG. 15. The reflection spectrum for different incident angles θ from 0° to 25°. (a) Before merge and (b) after merge at off-Γ. The resonance wavelength decreases with increasing incident angle.

ACKNOWLEDGMENTS

This paper was supported by National Key Research and Development Program of China (Grant No. 2021YFA1400602) and by the National Natural Science Foundation of China (Grants No. 11974261, No. 12104105, and No. 91850206).

APPENDIX A: COMPUTATIONAL METHODS

The dielectric pillars were designed to have radius of $r = 106$ nm and $h = 338$ nm, and the PhCS has a lattice constant of $a = 422$ nm in Fig. 1. The simulation domain is given by the unit cell, as shown in Fig. 12. The boundary conditions applied to the sides of the system were periodic boundary conditions with Floquet periodicity to perform calculations in the reciprocal space, while perfectly matched layers were applied to the top (air side) and bottom (air side), as depicted in the color scheme is Fig. 12. The numerical simulations were performed by commercially available software COMSOL, using the "Wave optics module" with "Electromagnetic waves, frequency domain" physics coupled to an eigenfrequency study with a direct solver (MUMPS). We set the mesh width in the dielectric cylinder to 3.38×10^{-10} m and an air box height much larger than the period a ($\sim 10a$) to ensure model convergence. For each electromagnetic mode found in the solutions, we analyzed the polarization of the fields to distinguish between TE and TM modes. The dielectric pillars refractive index was 3.48, which can be selected experimentally in silicon, gallium arsenide, and other materials.

APPENDIX B: FAR-FIELD POLARIZATION IN AN ENLARGED k SPACE

Here, we show the distribution of far-field polarization in an enlarged k space, as shown in Fig. 13. The structure parameters are $a = 435$ nm, $r = 106$ nm, and $h = 340$ nm. The white arrow is the far-field polarization plotted along the long axis of the ellipse polarization. The vortex and antivortex phenomena can be seen more clearly. The first accidental BIC exhibits an antivortex with a topological charge of -1, while the second accidental BIC exhibits a vortex with a topological charge of 1.

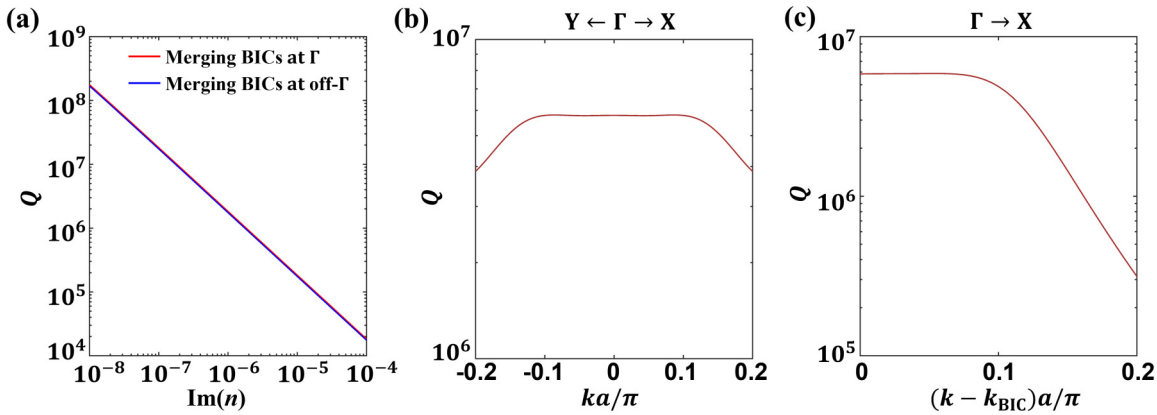

FIG. 16. The robustness of the merging bound states in the continuum (BICs) against intrinsic loss. (a) Influence of intrinsic loss on merging BICs. Simulation for the evolution of Q factors with different intrinsic loss of materials at merging BICs. The Q factors with intrinsic loss $\mathrm{Im}(n) = 10^{-6}$ for merging BIC at (b) the Γ point and (c) an off-Γ point. Other structural parameters stay the same as Figs. 2 and 7 for $a = 423.2$ and 421.1 nm, respectively.

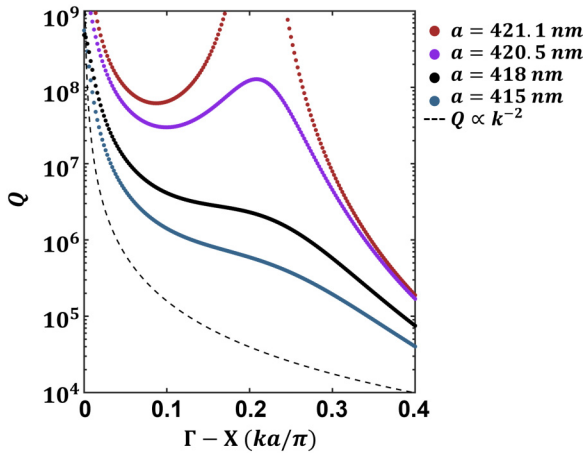

FIG. 17. Simulated Q factors with different lattice constants a. The dashed line represents the Q variation of an isolated bound state in the continuum (BIC) at the Γ point.

APPENDIX C: PROOF OF THE EXISTENCE OF MULTIPLE ACCIDENTAL BICs

We prove the existence of multiple accidental BICs by calculating the reflection angle spectrum. First, we calculated the angle spectrum before the merger, and the structure used the parameters in Fig. 1. It can be observed that a symmetry-protected BIC and accidental BICs cannot be observed in spectra with disappeared linewidths, as shown in Fig. 14. It worth noting that the resonance linewidth between BICs on the same band is very narrow and difficult to observe.

For clarity, the reflection spectra at different angles are shown in Fig. 15(a). The resonance wavelength decreases with increasing incidence angle. The resonance linewidth disappears at certain angles (black circle), which corresponds to different accidental BICs and symmetry-protected BICs. We can further confirm that two accidental BICs have opposite topological charges. Further reducing the periodic constant, no vanishing resonance linewidth can be observed on the reflection angle spectrum, as shown in Fig. 15(b). This is due to two incidental BICs approaching each other and annihilating, corresponding to Fig. 7. This change also proves that two accidental BICs have opposite topological charges.

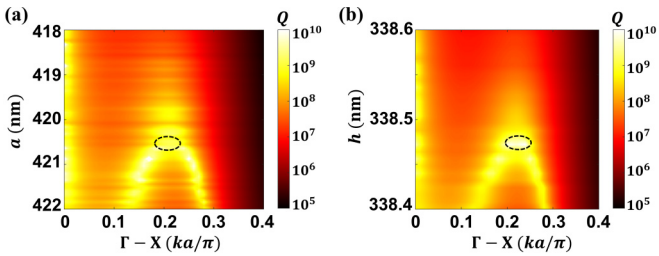

FIG. 18. Evolution of merging bound states in the continuum (BICs) at an off-Γ point with different structural parameters: (a) the periodic constant a, and (b) the height of cylinder h. The dotted circle represents the position of merging BICs. Other parameters are $h = 338.4$ nm in (a) and $a = 422$ nm in (b). The position of merging BICs can be steered by adjusting parameters a and h.

APPENDIX D: INTRINSIC LOSS OF MATERIALS

The loss of the system is mainly composed of intrinsic loss caused by materials and radiation loss, following $\gamma_{\text{Total}} = \gamma_{\text{in}} + \gamma_{\text{rad}}$. For merging BICs, the radiation loss is eliminated due to the destructive interference between radiation channels, which means that Q factors are dominated by the intrinsic loss of materials, as shown in Fig. 16(a). Therefore, dielectric materials with ultralow intrinsic loss, such as TiO_2 and Si_3N_4, are ideal choices to form a high-Q cavity in optical frequencies. In our designed merging BICs at Γ and off-Γ points, the Q factors are still sufficiently large in a broad wave vector range with an unavoidable intrinsic loss [$\text{Im}(n) = 10^{-6}$], as shown in Figs. 16(b) and 16(c).

APPENDIX E: ROBUSTNESS OF Q UNDER NONIDEAL FABRICATION CONDITIONS

Here, we discuss the impact of lattice constant perturbations a on the merging quasi-BIC quality factor, as shown in Fig. 17. When a changes from 421.1 to 420.5 nm, the two accidental BICs annihilate each other to form an ultrahigh-Q mode, called the supercavity mode. Further increasing the period constant a to 418 and 415 nm, the Q of the supercavity mode is still an order of magnitude higher than that of an isolated BIC (black dotted line; $Q \propto k^{-2}$). Therefore, the high-Q resonance caused by merging BICs is robust and can maintain high performance of enhanced GHS and sensor even if there is a disturbance of the lattice constant a due to nonideal fabrication.

APPENDIX F: EVOLUTION OF BICs WITH THE VARIATION OF STRUCTURAL PARAMETERS

The evolution of merging BICs at an off-Γ point with variation of the period a and the height h is shown in Fig. 18. The height h is fixed at 338.4 nm, and the period a is fixed at 422 nm in Figs. 18(a) and 18(b), respectively. When we continuously change the parameters, the trajectory of BICs is visible in the momentum space. With decreasing the period or increasing the height, two accidental BICs approach each other. If the parameters are further changed, they will be annihilated and transformed into a quasi-BIC with a finite Q factor due to the opposite topological charges of two BICs. It is worth noting that the position of a merging BIC formed by adjusting different parameters is slightly different, as indicated of the dotted circle in Figs. 18(a) and 18(b). That means, with changing different parameters, the moving speed of two accidental BICs in momentum space is different. Thus, we can adjust these two parameters (a and h) simultaneously to realize merging BICs at any wave vector position, as shown in Fig. 8.

APPENDIX G: REFLECTANCE ANGULAR SPECTRA FOR QUASI-BIC

Here, fixing the incident wavelength λ_0 near the resonance in Fig. 9(b), we calculate the reflectance angular spectra and reflection phase angular spectra when the peak value of GHS occurs at 5°, 10°, 20°, and 25°, respectively, as shown in

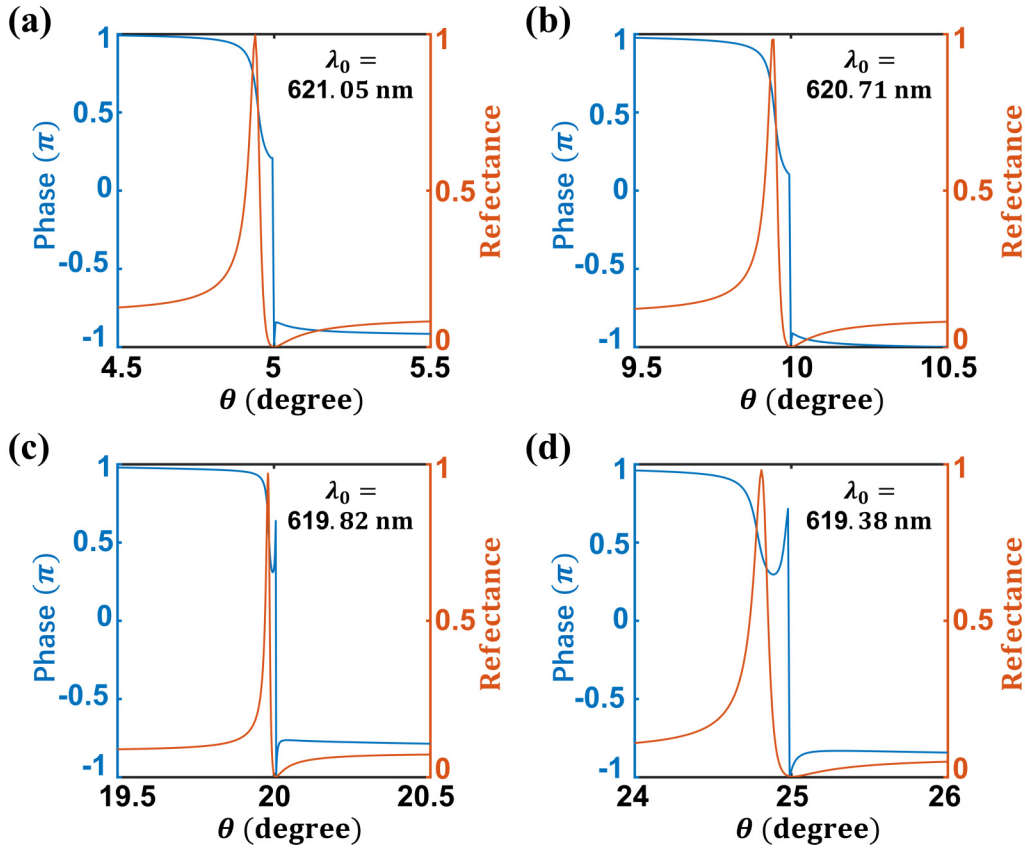

FIG. 19. Enhanced Goos-Hänchen shift (GHS) assisted by off-Γ merging bound states in the continuum (BICs). The reflectance angular spectra (orange line) and phase angular spectra (blue line) for (a) $\lambda_0 = 621.05$ nm, (b) $\lambda_0 = 620.71$ nm, (c) $\lambda_0 = 619.82$ nm, and (d) $\lambda_0 = 619.38$ nm.

Fig. 19. At the reflectance dip, there will be a drastic change in phase, resulting in a giant GHS. The Q factors of a quasi-BIC in a large wave vector range near a merging BIC are very high. Therefore, whether the giant GHS occurs at 5°, 10°, 20°, or 25°, the reflectance angular spectrum always keeps a very narrow linewidth. Meanwhile, when the peak value of GHS changes from 5° to 25°, the relative shift is only 0.27%. Therefore, utilizing merging BICs at an off-Γ point can also realize wide-angle GHS enhancement within an extremely narrow bandwidth.

[1] F. Goos and H. Hänchen, Ein neuer und fundamentaler Versuch zur Totalreflexion, Ann. Phys. **436**, 333 (1947).

[2] K. Artmann, Berechnung der Seitenversetzung des totalreflektierten Strahles, Ann. Phys. **437**, 87 (1948).

[3] K. L. Tsakmakidis, A. D. Boardman, and O. Hess, 'Trapped rainbow' storage of light in metamaterials, Nature (London) **450**, 397 (2007).

[4] Z. Liu, F. Lu, L. Jiang, W. Lin, and Z. Zheng, Tunable Goos-Hänchen shift surface plasmon resonance sensor based on graphene-hBN heterostructure, Biosensors **11**, 201 (2021).

[5] Q. Ji, B. Yan, L. Han, J. Wang, M. Yang, and C. Wu, Theoretical investigation of an enhanced Goos-Hanchen shift sensor based on a BlueP/TMDC/graphene hybrid, Appl. Opt. **59**, 8355 (2020).

[6] X. M. Chen, T. Shui, C. Meng, T. Zhang, X. Deng, and W. X. Yang, Controllable Goos-Hänchen shift and optical switching in an Er^{3+}−doped yttrium aluminum garnet crystal, Laser Phys. Lett. **18**, 045205 (2021).

[7] X. Wang, C. Yin, J. Sun, J. Gao, M. Huang, and Z. Cao, Reflection-type space-division optical switch based on the electrically tuned Goos-Hänchen effect, J. Opt. **15**, 014007 (2013).

[8] X. Chen, M. Shen, Z. F. Zhang, and C. F. Li, Tunable lateral shift and polarization beam splitting of the transmitted light beam through electro-optic crystals, J. Appl. Phys. **104**, 123101 (2008).

[9] H. M. Lai and S. W. Chan, Large and negative Goos-Hänchen shift near the Brewster dip on reflection from weakly absorbing media, Opt. Lett. **27**, 680 (2002).

[10] Y. Y. Huang, W. T. Dong, L. Gao, and C. W. Qiu, Large positive and negative lateral shifts near pseudo-Brewster dip on reflection from a chiral metamaterial slab, Opt. Express **19**, 1310 (2011).

[11] C. Xu, J. Xu, G. Song, C. Zhu, Y. Yang, and G. S. Agarwal, Enhanced displacements in reflected beams at hyperbolic metamaterials, Opt. Express **24**, 21767 (2016).

[12] R. Kaiser, Y. Levy, J. Fleming, S. Muniz, and V. S. Bagnato, Resonances in a single thin dielectric layer: Enhancement of the Goos-Hänchen shift, Pure Appl. Opt. **5**, 891 (1996).

[13] Q. You, Y. Shan, S. Gan, Y. Zhao, X. Dai, and Y. Xiang, Giant and controllable Goos-Hänchen shifts based on surface plasmon resonance with graphene−MoS_2 heterostructure, Opt. Mater. Express **8**, 3036 (2018).

[14] L. G. Wang and S. Y. Zhu, Giant lateral shift of a light beam at the defect mode in one-dimensional photonic crystals, Opt. Lett. **31**, 101 (2006).

[15] J. Wen, J. Zhang, L. G. Wang, and S. Y. Zhu, Goos-Hänchen shifts in an epsilon-near-zero slab, J. Opt. Soc. Am. B **34**, 2310 (2017).

[16] H. Wu, Q. Luo, H. Chen, Y. Han, X. Yu, and S. Liu, Magnetically controllable nonreciprocal Goos-Hänchen shift supported by a magnetic plasmonic gradient metasurface, Phys. Rev. A **99**, 033820 (2019).

[17] K. Koshelev, G. Favraud, A. Bogdanov, Y. Kivshar, and A. Fratalocchi, Nonradiating photonics with resonant dielectric nanostructures, Nanophotonics **8**, 725 (2019).

[18] C. W. Hsu, B. Zhen, A. D. Stone, J. D. Joannopoulos, and M. Soljačić, Bound states in the continuum, Nat. Rev. Mater. **1**, 16048 (2016).

[19] A. F. Sadreev, Interference traps waves in an open system: Bound states in the continuum, Rep. Prog. Phys. **84**, 055901 (2021).

[20] H. Friedrich and D. Wintgen, Interfering resonances and bound states in the continuum, Phys. Rev. A **32**, 3231 (1985).

[21] G. Corrielli, G. Della Valle, A. Crespi, R. Osellame, and S. Longhi, Observation of surface states with algebraic localization, Phys. Rev. Lett. **111**, 220403 (2013).

[22] M. I. Molina, A. E. Miroshnichenko, and Y. S. Kivshar, Surface bound states in the continuum, Phys. Rev. Lett. **108**, 070401 (2012).

[23] L. Huang, B. Jia, Y. K. Chiang, S. Huang, C. Shen, F. Deng, T. Yang, D. A. Powell, Y. Li, and A. E. Miroshnichenko, Topological supercavity resonances in the finite system, Adv. Sci. **9**, 2200257 (2022).

[24] I. Deriy, I. Toftul, M. Petrov, and A. Bogdanov, Bound states in the continuum in compact acoustic resonators, Phys. Rev. Lett. **128**, 084301 (2022).

[25] L. Huang, Y. K. Chiang, S. Huang, C. Shen, F. Deng, Y. Cheng, B. Jia, Y. Li, D. A. Powell, and A. E. Miroshnichenko, Sound trapping in an open resonator, Nat. Commun. **12**, 4819 (2021).

[26] P. J. Cobelli, V. Pagneux, A. Maurel, and P. Petitjeans, Experimental study on water-wave trapped modes, J. Fluid Mech. **666**, 445 (2011).

[27] H. Qin, Z. Su, M. Liu, Y. Zeng, M. C. Tang, M. Li, Y. Shi, W. Huang, C. W. Qiu, and Q. Song, Arbitrarily polarized bound states in the continuum with twisted photonic crystal slabs, Light Sci. Appl. **12**, 66 (2023).

[28] P. Vaity, H. Gupta, A. Kala, S. Dutta Gupta, Y. S. Kivshar, V. R. Tuz, and V. G. Achanta, Polarization-independent quasi-bound states in the continuum, Adv. Photonics Res. **3**, 2100144 (2021).

[29] J. Wu, X. Xu, X. Su, S. Zhao, C. Wu, Y. Sun, Y. Li, F. Wu, Z. Guo, H. Jiang, and H. Chen, Observation of giant extrinsic chirality empowered by quasi-bound states in the continuum, Phys. Rev. Appl. **16**, 064018 (2021).

[30] Y. Lin, T. Feng, S. Lan, J. Liu, and Y. Xu, On-chip diffraction-free beam guiding beyond the light cone, Phys. Rev. Appl. **13**, 064032 (2020).

[31] Z. Zhang, F. Qin, Y. Xu, S. Fu, Y. Wang, and Y. Qin, Negative refraction mediated by bound states in the continuum, Photon. Res. **9**, 1592 (2021).

[32] P. Hu, C. Xie, Q. Song, A. Chen, H. Xiang, D. Han, and J. Zi, Bound states in the continuum based on the total internal reflection of Bloch waves, Natl. Sci. Rev. **10**, nwac043 (2023).

[33] P. Hu, J. Wang, Q. Jiang, J. Wang, L. Shi, D. Han, Z. Q. Zhang, C. T. Chan, and J. Zi, Global phase diagram of bound states in the continuum, Optica **9**, 1353 (2022).

[34] J. Wang, L. Shi, and J. Zi, Spin Hall effect of light via momentum-space topological vortices around bound states in the continuum, Phys. Rev. Lett. **129**, 236101 (2022).

[35] W. Liu, B. Wang, Y. Zhang, J. Wang, M. Zhao, F. Guan, X. Liu, L. Shi, and J. Zi, Circularly polarized states spawning from bound states in the continuum, Phys. Rev. Lett. **123**, 116104 (2019).

[36] B. Wang, W. Liu, M. Zhao, J. Wang, Y. Zhang, A. Chen, F. Guan, X. Liu, L. Shi, and J. Zi, Generating optical vortex beams by momentum-space polarization vortices centred at bound states in the continuum, Nat. Photon. **14**, 623 (2020).

[37] Q. Song, J. Hu, S. Dai, C. Zheng, D. Han, J. Zi, Z. Q. Zhang, and C. T. Chan, Coexistence of a new type of bound state in the continuum and a lasing threshold mode induced by PT symmetry, Sci. Adv. **6**, eabc1160 (2020).

[38] K. Koshelev, S. Lepeshov, M. Liu, A. Bogdanov, and Y. Kivshar, Asymmetric metasurfaces with high-Q resonances governed by bound states in the continuum, Phys. Rev. Lett. **121**, 193903 (2018).

[39] Q. Song, M. Zhao, L. Liu, J. Chai, G. He, H. Xiang, D. Han, and J. Zi, Observation of bound states in the continuum in the dimerized chain, Phys. Rev. A **100**, 023810 (2019).

[40] Z. Sadrieva, K. Frizyuk, M. Petrov, Y. Kivshar, and A. Bogdanov, Multipolar origin of bound states in the continuum, Phys. Rev. B **100**, 115303 (2019).

[41] M. S. Sidorenko, O. N. Sergaeva, Z. F. Sadrieva, C. Roques-Carmes, P. S. Muraev, D. N. Maksimov, and A. A. Bogdanov, Observation of an accidental bound state in the continuum in a chain of dielectric disks, Phys. Rev. Appl. **15**, 034041 (2021).

[42] D. R. Abujetas, J. Olmos-Trigo, and J. A. Sánchez-Gil, Tailoring accidental double bound states in the continuum in all-dielectric metasurfaces, Adv. Opt. Mater. **10**, 2200301 (2022).

[43] F. Yesilkoy, E. R. Arvelo, Y. Jahani, M. Liu, A. Tittl, V. Cevher, Y. Kivshar, and H. Altug, Ultrasensitive hyperspectral imaging and biodetection enabled by dielectric metasurfaces, Nat. Photonics **13**, 390 (2019).

[44] Z. Li, Y. Xiang, S. Xu, and X. Dai, Ultrasensitive terahertz sensing in all-dielectric asymmetric metasurfaces based on quasi-BIC, J. Opt. Soc. Am. B **39**, 286 (2021).

[45] K. Koshelev, S. Kruk, E. Melik-Gaykazyan, J. H. Choi, A. Bogdanov, H. G. Park, and Y. Kivshar, Subwavelength dielectric resonators for nonlinear nanophotonics, Science **367**, 288 (2020).

[46] Z. Liu, Y. Xu, Y. Lin, J. Xiang, T. Feng, Q. Cao, J. Li, S. Lan, and J. Liu, High-Q quasibound states in the continuum for nonlinear metasurfaces, Phys. Rev. Lett. **123**, 253901 (2019).

[47] V. Kravtsov, E. Khestanova, F. A. Benimetskiy, T. Ivanova, A. K. Samusev, I. S. Sinev, D. Pidgayko, A. M. Mozharov, I. S. Mukhin, M. S. Lozhkin *et al.*, Nonlinear polaritons in a monolayer semiconductor coupled to optical bound states in the continuum, Light Sci. Appl. **9**, 56 (2020).

[48] R. Masoudian Saadabad, L. Huang, and A. E. Miroshnichenko, Polarization-independent perfect absorber enabled by quasi-bound states in the continuum, Phys. Rev. B **104**, 235405 (2021).

[49] E. Gao, H. Li, Z. Liu, C. Xiong, C. Liu, B. Ruan, M. Li, and B. Zhang, Investigation of bound states in the continuum in dual-band perfect absorbers, Opt. Express **30**, 14817 (2022).

[50] C. Huang, C. Zhang, S. Xiao, Y. Wang, Y. Fan, Y. Liu, N. Zhang, G. Qu, H. Ji, J. Han *et al.*, Ultrafast control of vortex microlasers, Science **367**, 1018 (2020).

[51] Y. Yu, A. Sakanas, A. R. Zali, E. Semenova, K. Yvind, and J. Mørk, Ultra-coherent Fano laser based on a bound state in the continuum, Nat. Photon. **15**, 758 (2021).

[52] M. S. Hwang, H. C. Lee, K. H. Kim, K. Y. Jeong, S. H. Kwon, K. Koshelev, Y. Kivshar, and H. G. Park, Ultralow-threshold laser using super-bound states in the continuum, Nat. Commun. **12**, 4135 (2021).

[53] Y. Ruan, Y. Li, Z. Hu, J. Wang, and Y. Wang, Strong resonance response with ultrahigh quality factor in grating-multilayer systems based on quasi-bound states in the continuum, Sci. Rep. **12**, 21471 (2022).

[54] F. Wu, J. Wu, Z. Guo, H. Jiang, Y. Sun, Y. Li, J. Ren, and H. Chen, Giant enhancement of the Goos-Hänchen shift assisted by quasibound states in the continuum, Phys. Rev. Appl. **12**, 014028 (2019).

[55] F. Wu, M. Luo, J. Wu, C. Fan, X. Qi, Y. Jian, D. Liu, S. Xiao, G. Chen, H. Jiang *et al.*, Dual quasibound states in the continuum in compound grating waveguide structures for large positive and negative Goos-Hänchen shifts with perfect reflection, Phys. Rev. A **104**, 023518 (2021).

[56] Z. Zheng, Y. Zhu, J. Duan, M. Qin, F. Wu, and S. Xiao, Enhancing Goos-Hanchen shift based on magnetic dipole quasi-bound states in the continuum in all-dielectric metasurfaces, Opt. Express **29**, 29541 (2021).

[57] S. Du, W. Zhang, W. Liu, Y. Zhang, M. Zhao, and L. Shi, Realization of large transmitted optical Goos-Hänchen shifts in photonic crystal slabs, Nanophotonics **11**, 4531 (2022).

[58] S. Sinha Biswas, G. Remesh, V. G. Achanta, A. Banerjee, N. Ghosh, and S. Dutta Gupta, Enhanced beam shifts mediated by bound states in continuum, J. Opt. **25**, 095401 (2023).

[59] Z. Huang, W. Liu, Z. Wei, H. Meng, H. Liu, J. Guo, Y. Zhi, L. Xiang, H. Li, and F. Wang, Giant enhancement of the Goos-Hanchen shift based on quasi-bound states in the continuum in terahertz band through silicon based metasurface, Opt. Commun. **540**, 129507 (2023).

[60] J. Jin, X. Yin, L. Ni, M. Soljacic, B. Zhen, and C. Peng, Topologically enabled ultrahigh-Q guided resonances robust to out-of-plane scattering, Nature (London) **574**, 501 (2019).

[61] S. Wan, K. Wang, F. Wang, C. Guan, W. Li, J. Liu, A. Bogdanov, P. A. Belov, and J. Shi, Topologically enabled ultrahigh-Q chiroptical resonances by merging bound states in the continuum, Opt. Lett. **47**, 3291 (2022).

[62] H. Barkaoui, K. Du, Y. Chen, S. Xiao, and Q. Song, Merged bound states in the continuum for giant superchiral field and chiral mode splitting, Phys. Rev. B **107**, 045305 (2023).

[63] M. Kang, S. Zhang, M. Xiao, and H. Xu, Merging bound states in the continuum at off-high symmetry points, Phys. Rev. Lett. **126**, 117402 (2021).

[64] M. Kang, L. Mao, S. Zhang, M. Xiao, H. Xu, and C. T. Chan, Merging bound states in the continuum by harnessing higher-order topological charges, Light Sci. Appl. **11**, 228 (2022).

[65] S. Chen, Z. Li, Y. Mao, X. Dai, and Y. Xiang, Giant enhancement of the Goos-Hänchen shift assisted by merging bound states in the continuum, J. Appl. Phys. **133**, 193101 (2023).

[66] B. Zhen, C. W. Hsu, L. Lu, A. D. Stone, and M. Soljačić, Topological nature of optical bound states in the continuum, Phys. Rev. Lett. **113**, 257401 (2014).

[67] A. Pawlowski, J. L. Guzman, F. Rodríguez, M. Berenguel, J. Sánchez, and S. Dormido, Simulation of greenhouse climate monitoring and control with wireless sensor network and event-based control, Sensors **9**, 232 (2009).

[68] Y. Chen, W. Ji, K. Yan, J. Gao, and J. Zhang, Fuel cell-based self-powered electrochemical sensors for biochemical detection, Nano Energy **61**, 173 (2019).

[69] L. Xiang, Z. Zhu, J. Tian, and Y. Tian, Foreign object detection in a wireless power transfer system using symmetrical coil sets, IEEE Access **7**, 44622 (2019).

[70] D. T. F. Marple, Refractive index of GaAs, J. Appl. Phys. **35**, 1241 (1964).

[71] D. Pogany, N. Seliger, E. Gornik, M. Stoisiek, and T. Lalinský, Analysis of the temperature evolution from the time resolved thermo-optical interferometric measurements with few Fabry-Pérot peaks, J. Appl. Phys. **84**, 4495 (1998).